Computationally-validated surrogate models for optimal geometric design of bio-inspired swimming robots: Helical swimmers

A.F. Tabak [a,*], S. Yesilyurt [b,1]

[a] Mechatronics Program, Faculty of Engineering and Design, Istanbul Commerce University, Kucukyali, Istanbul, Turkey
[b] Mechatronics Program, Faculty of Engineering and Natural Sciences, Sabanci University, Tuzla, Istanbul, Turkey

ARTICLE INFO

ABSTRACT

Research on micro-swimming robots without tether is growing fast owing to their potential impact on minimally invasive medical procedures. Candidate propulsion mechanisms of robots are vastly based on micro-organisms with rotating helical tails. For design of swimming robots, accurate models are necessary to compute velocities with corresponding hydrodynamic forces. Resistive force theory (RFT) provides an excellent framework for six degrees-of-freedom (dof) surrogate models in order to carry out effective design studies. However, resistance coefficients reported in literature are based on approximate analytical solutions for asymptotical cases, and do not address the effect of hydrodynamic interactions between the body and the tail, even in unbounded fluid media. Here, we use hydrodynamic interaction coefficients that multiply the body resistance coefficients along with no further modification to local resistance coefficients of the tail. Interaction coefficients are obtained from the solution of the inverse problem once for a fixed representative design with a computational fluid dynamics (CFD) simulation or an experiment. Results of the RFT-based hydrodynamic model are compared against further CFD simulations, and indicate that the model with hydrodynamic interaction coefficients obtained from a representative design provides a viable surrogate for computationally intensive three-dimensional time-dependent CFD models for a range of design variables. Finally, the validated hydrodynamic model is employed to investigate efficient geometric designs with helical wave propagation method within a wider range of design parameters.

1. Introduction

Potential advantages of micro-swimming robots can revolutionize the modern medicine: procedures such as kidney stone destruction, cleaning of clogged arteries, reaching tumors deep inside vital organs or retina restoration can be performed with minimal side-effects [1,2]. Conventional mechanisms such as propellers cannot achieve propulsion at low Reynolds numbers in simple fluids, such as in micro-fluids, as stated by Purcell's scallop theorem [3]. However, propulsion mechanisms of natural micro-swimmers are viable candidates for propulsion of autonomous micro-swimming robots [4]. Bio-inspired propulsion mechanisms with helical wave propagation have been demonstrated in literature: here, a representative review is presented.

Zhang et al. [5,6] manufactured artificial helical flagella as small as a few tens of microns long. Metal and polymer layers are deposited in the shape of a narrow tape and formed into a helix due to the tensile stress exerted on the inner layers during the manufacturing process. A magnetic bead of 4.5 × 4.5 × 0.2 cubic micrometers is attached to one end of the artificial flagellum. In the presence of a rotating external magnetic field, the torque on the magnetic head enabled the rotation of the helical flagellum and the forward motion of the artificial swimmer. Ghosh and Fischer [7] demonstrated the use of glancing angle deposition on the silicon wafer in an electron beam evaporator to obtain about a micro-scale helical screw like structures with diameters of a few hundreds of nanometers. In that study, helical structures are removed from the wafer, laid onto a surface and deposited by magnetic cobalt on one side. By means of a tri-axial Helmholtz coil, a rotating magnetic field is generated and modified by an open loop control scheme to navigate the micro-robot on a preselected path.

Furthermore, there are *in vitro* studies directly incorporating bacteria species in computer controlled tasks as cargo carriers: Martel et al. [8] and Martel and Mohammadi [9] carried out exper-

* Corresponding author. Tel.: +90 2164891888/3325, fax: +90 2164890269.
    E-mail addresses: aftabak@ticaret.edu.tr (A.F. Tabak), syesilyurt@sabanciuniv.edu (S. Yesilyurt).
   [1] Tel.: +90 2164839579; fax: +90 2164839550.

iments with magnetotactic bacteria (MTB) species, which use earths' magnetic field to control their swimming path, and demonstrated that with an induced magnetic field it is possible to control MTBs as individuals or as a swarm to tow micro-scale objects. These studies are particularly important to demonstrate the possibility of using actual bacteria for a predefined task for which the feasibility of deploying an artificial swimmer is unlikely due to mission parameters or environmental conditions.

Hydrodynamic models of the propulsion of micro-organisms by means of resistance coefficients have been studied for over sixty years. Gray and Hancock [10] presented the application of resistance coefficients to calculate fluid forces due to time-irreversible motion of slender filaments. Force coefficients are obtained from the approximate solution of the fluid motion represented by local singularities, i.e., Stokeslet functions representing local point forces, on the filament [11]. Lighthill [12] used the slender body theory (SBT) based on the velocity field represented by distribution of point forces on the helical tail of the swimmers. Higdon [13] used a numerical integration method for the integrals approximated by Lighthill to calculate the velocity of a swimmer with a spherical head and a helical tail, and reported the variation of the swimming velocity with the tail length, wavelength and amplitude given in dimensionless forms with respect to the diameter of the body.

Numerical solutions of the flow coupled with the equation of motion of the swimmer are carried out extensively in literature. Ramia et al. [14] obtained instantaneous velocities of swimming of micro-organisms from the solution of Stokes equations with the boundary element method (BEM) in order to study hydrodynamic interactions between cells and solid boundaries as well as the interaction between the body and the tail of a cell. Goto et al. [15] employed BEM for the solution of Stokes equations, calculated the velocity vector of a natural micro-swimmer, compared their results with observations of swimming bacteria, *Vibrio alginolyticus*, and concluded that the BEM solutions agree reasonably well with observations.

Design of bio-inspired micro-swimming robots can benefit from accurate hydrodynamic models that predict forward and lateral velocities of robots. It has been demonstrated that RFT can be used to develop real-time models to predict the full three-dimensional trajectory of micro-swimmers [16,17]: in RFT models, hydrodynamic forces on a flagellum are calculated from resistance coefficients, and drag forces on bodies are obtained from analytical relationships for simple objects in viscous mediums. Models that use several variants of resistance coefficients do not yield accurate predictions for even the forward velocity of a swimmer for all configurations of flagellum parameters in the presence of a sizable body of the swimmer compared to the tail [17–20]. The hydrodynamic interaction between the body and the tail is one of the key phenomena which are not included properly in RFT models. Lighthill [12] included the effect of the cell body on the SBT-based calculations of the velocity of the swimmer and concluded that the correction is very small compared to an isolated infinite flagellum. Chattopadhyay and Wu [20] demonstrated that Lighthill's correction is insufficient for micro-swimming species such as *V. alginolyticus*. Furthermore hydrodynamic interaction between the body and the flagellum was studied numerically by Ramia et al. [14], and authors concluded that the presence of the cell body does not alter the propulsion force of the flagellum significantly. However, authors did not provide detailed results for the effect of flagellum on the drag force on the body of the cell compared to an isolated body with the same shape and size.

Hydrodynamic forces on tails are obtained from the integration of local forces in tangent and perpendicular directions to the motion and expressed by resistance coefficients over the tail. Force coefficients can be calculated from analytical formulas available in the literature, such as from Lighthill's SBT analysis [12]. Body resistance coefficients are known for isolated objects such as spheroids in unbounded fluid media: for example, the resistance coefficient is $F_i/U_i = -6\pi\mu a$ for the fluid force F_i acting on an isolated spherical object of radius a moving with velocity U_i in an unbounded fluid of viscosity μ in an arbitrary direction [21,22].

We propose hydrodynamic interaction coefficients, γ_i, which scale the resistance coefficient for the motion in an arbitrary ith direction, i.e., $F_i/U_i = -\gamma_i 6\pi\mu a$. Hydrodynamic interaction coefficients are different for each direction due to the rotation of the helical tail, which breaks the symmetry of the flow over the spherical body. Accurate calculation of hydrodynamic interactions is extremely difficult analytically; however, an experiment or a single CFD simulation can be performed for a fixed representative design in order to obtain a set of necessary coefficients.

The inverse problem is solved only once with a single CFD-simulation for a representative design with fixed design variables to obtain unknown force coefficients and corrections. The method is somewhat ad-hoc in prediction of hydrodynamic interaction coefficients for the sake of improving the accuracy of the RFT model which takes seconds to run instead of hours in the case of three-dimensional CFD simulations subject to free-swimming constraints.

Main contributions of this study are to obtain a particular constant set of resistance coefficients with corrections embedded to account for the effect of hydrodynamic interactions on the body for a representative design, with the help of a single CFD simulation, and use them in a model with reduced numerical stiffness offering a simple and fast computational tool, which will provide reliable calculations of time-averaged swimming velocities in a predefined neighborhood around the representative design suitable for design-optimization purposes. Therefore, the RFT-based simple model presented here serves as a surrogate for accurate numerical models, such as computationally intensive and time demanding finite element or boundary element simulations, and can be used in design optimization studies to search alternative designs in the neighborhood of the representative design.

To that end, the RFT model, which is incorporated with hydrodynamic interaction corrections for the body and constant resistance coefficients for the tail, is validated with measurements of Goto et al. [15] for a group of species of micro-organisms with varying body and tail dimensions, and with three-dimensional time-dependent CFD simulation experiments for swimmers with geometric designs different than the representative model used to obtain interaction coefficients. Furthermore, the validated hydrodynamic model is used to obtain optimal efficient tail parameters for desired operations such as efficiency and speed within a predefined design space with a regular grid to demonstrate its advantage over conventional numerical simulation methods.

2. Methodology

2.1. Hydrodynamic model

Velocity vector of a two-link micro-swimmer is obtained from the equation of motion [17,23], which balances forces on the swimmer's body and the tail:

$$F_{body} + F_{tail} = 0 \tag{1}$$

where $F = [\mathbf{F}', \mathbf{T}']'$ is the generalized force vector, $\mathbf{F}$ and $\mathbf{T}$ are force and torque vectors, "$'$" is the transpose, and body and tail forces are referred with respective subscripts "*body*" and "*tail*". For simplicity, we assume that the body of the swimmer is a blunt object such as a sphere, and the tail is subject to a helical wave

propagation motion, i.e., rotation, which generates propulsion force in viscous flows as observed among micro-swimming organisms.

For creeping flows equations of motion can be cast in a linear system of equations relating the generalized force and velocity vectors by means of the resistance matrix, $\mathbf{B}_i$, as follows:

$$F_i = -\mathbf{B}_i\mathbf{V}_i. \tag{2}$$

Here, $i = \{body, tail\}$, $\mathbf{V} = [\mathbf{U}'\ \mathbf{\Omega}']'$ is the generalized velocity vector; $\mathbf{U}$ and $\mathbf{\Omega}$ are translational and rotational velocity vectors respectively.

The resistance matrix for the body of the swimmer [17], $\mathbf{B}_{body}$, is simpler than the resistance matrix of tail and obtained from the linear and rotational resistances of the body, thus, can be considered as a combination of four subcomponents which relate linear and angular velocities to forces and torques:

$$\mathbf{B}_{body} = \begin{bmatrix} \mathbf{D}_N & \mathbf{E} \\ \mathbf{E}' & \mathbf{D}_R \end{bmatrix}. \tag{3}$$

In Eq. (3), $\mathbf{D}_N$ and $\mathbf{D}_R$ are 3×3 diagonal matrices signifying the translational and rotational resistances of the body, $\mathbf{E}$, which contains nonzero elements should centers of geometry of body and swimmer be far apart.

For a spherical isolated body in an unbounded fluid, each diagonal element of $\mathbf{D}_N$ is $6\pi\mu r_{body}$ and each diagonal element of $\mathbf{D}_R$ is $8\pi\mu(r_{body})^3$, where μ is the dynamic viscosity and r_{body} is the radius of the spherical body [21,22]. However, even for a simple body such as a sphere, resistance matrices $\mathbf{D}_N$ and $\mathbf{D}_R$ must be modified due to motion of the tail attached to the body as well as for flows inside channels and nearby boundaries [24,25]. In effect, the interaction coefficients are only applied to the body resistances and they need to be estimated well in order to ensure accuracy of the hydrodynamic model.

Time-dependent resistance matrix of the tail [17], $\mathbf{B}_{tail}$ in Eq. (2), is obtained by integration over local forces:

$$\mathbf{B}_{tail} = \int_0^L \begin{bmatrix} \mathbf{RCR}' & -\mathbf{RCR}'\mathbf{S} \\ \mathbf{SRCR}' & -\mathbf{SRCR}'\mathbf{S} \end{bmatrix} \alpha\, ds \tag{4}$$

where α is the ratio between apparent and actual lengths of the tail, L is the apparent length of the tail in the **s**-direction, $\mathbf{S}$ is the skew-symmetric matrix that corresponds to the cross product with the position vector on the tail, $\mathbf{R}$ is the rotation matrix from the local Frenet–Serret frames with local tangential, **t**, bi-normal, **b**, and normal, **n**, vectors [26], and the **sqr**-coordinate frame of the swimmer and signified as position, s, and time, t, dependent functions as $\mathbf{R} = [\mathbf{t}(s,t)\ \mathbf{n}(s,t)\ \mathbf{b}(s,t)]$ (see Fig. 1).

The local resistance matrix at a given position on the tail, signified by $\mathbf{C}$ in Eq. (4), is a diagonal matrix of local resistance coefficients in the tangent, c_t, bi-normal and normal directions, $c_{\{n,b\}}$. Local resistance coefficients are assumed identical in the bi-normal
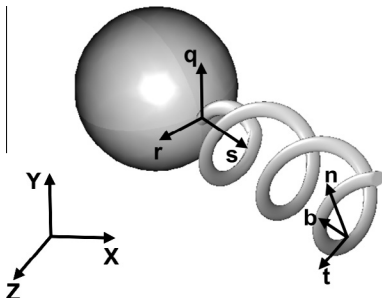

Fig. 1. Swimmer with a rotating helical tail: **XYZ** is the stationary frame; **sqr** is located at the joint and translates with the body; and **tnb** denotes the local time-dependent Frenet–Serret coordinates on the tail.

and normal directions due to the symmetry of the induced flow field.

Accurate calculation of the resistance coefficients is extremely difficult. Lighthill [12] derived resistance coefficients from the distribution of point forces on an infinite helix in an unbounded fluid, and the local normal and tangential components of the resistance coefficients are obtained as follows:

$$c_{\{n,b\}} = \frac{4\pi\mu}{-\ln\ \varepsilon + (2\alpha^2 - 1)A_1 + 2(1 - \alpha^2)A_2}, \tag{5}$$

$$c_t = \frac{2\pi\mu}{-\ln\ \varepsilon - 0.5 + \alpha^2 A_1 + (1 - \alpha^2)A_2}. \tag{6}$$

Here, ε is given by $\varepsilon = 5.2a\alpha/\lambda$, where a denotes the filament radius of the tail, and λ is the wavelength. A_1 and A_2 are periodic integrals of the functions of assumed local flow field along the helical tail, which are discussed by Lighthill [12] in great detail.

Local velocity on the tail is the summation of the swimmer's net velocity and the motion of the tail with respect to the **sqr**-frame in Fig. 1:

$$\mathbf{U}_{tail} = \mathbf{U}_{body} + \hat{\mathbf{u}} \tag{7}$$

where $\hat{\mathbf{u}}$ is the local velocity on the tail, and can be obtained from or the rotation of the tail with $\hat{\mathbf{u}} = [\omega\ 0\ 0]' \times \mathbf{P}$, where $\omega = 2\pi f$, and f denotes the actuation frequency of the tail. For example for a left-handed helical tail as shown in Fig. 1, the position vector $\mathbf{P}$ is specified in the **sqr**-coordinate frame as follows:

$$\mathbf{P} = \begin{bmatrix} s \\ q(s,t) \\ r(s,t) \end{bmatrix} = \begin{bmatrix} s \\ b_s(s)\cos(ks - \omega t) \\ -b_s(s)\sin(ks - \omega t) \end{bmatrix}. \tag{8}$$

where k is the wave number and $b_s(s)$ is the local radius of the helix, which is modified with a ramp function to ensure a fixed connection with the body (see Fig. 1), e.g. $b_s(s) = 10b(s/L)$ for $s/L < 0.1$ and $b_s(s) = b$ for $(s/L) \geqslant 0.1$.

Forces on the tail can be decomposed into propulsion and drag forces. According to the linear relations given by Eqs. (2) and (7), then, we have:

$$\begin{bmatrix} \mathbf{F} \\ \mathbf{T} \end{bmatrix}_{tail} = -\mathbf{B}_{tail}\begin{bmatrix} \mathbf{U} \\ \mathbf{\Omega} \end{bmatrix}_{tail} = -\mathbf{B}_{tail}\left(\begin{bmatrix} \mathbf{U} \\ \mathbf{\Omega} \end{bmatrix}_{body} + \hat{\mathbf{u}}\right) = -\mathbf{B}_{tail}\begin{bmatrix} \mathbf{U} \\ \mathbf{\Omega} \end{bmatrix}_{body} - \begin{bmatrix} \mathbf{F}_p \\ \mathbf{T}_p \end{bmatrix}. \tag{9}$$

The first term in the right-hand-side of Eq. (9) is the total drag force on the tail due to its motion with the body, and the second term is the propulsion force, $\mathbf{F}_p$, and propulsion torque, $\mathbf{T}_p$, generated by the tail due to its motion relative to the body, and obtained from Eq. (4) as follows:

$$\begin{bmatrix} \mathbf{F}_p \\ \mathbf{T}_p \end{bmatrix} = \int_0^L \begin{bmatrix} \mathbf{RCR}\hat{\mathbf{u}} \\ (\mathbf{P} - \mathbf{P}_{com}) \times (\mathbf{RCR}\hat{\mathbf{u}}) \end{bmatrix} ds \tag{10}$$

where $\mathbf{C}$ denotes the local resistance matrix, and $\mathbf{P}_{com}$ is the position of the center of mass of the swimmer in **sqr**-coordinates.

Substituting Eqs. (2)–(4) and Eq. (9) into Eq. (1), one obtains the instantaneous velocity vector of the swimmer in the **sqr**-coordinates:

$$\begin{bmatrix} \mathbf{U}_{body} \\ \mathbf{\Omega}_{body} \end{bmatrix} = \left(\mathbf{B}_{body} + \mathbf{B}_{tail}\right)^{-1}\begin{bmatrix} \mathbf{F}_p \\ \mathbf{T}_p \end{bmatrix}. \tag{11}$$

2.2. CFD model

CFD model is used to compute reliable fluid forces especially at low Reynolds number flows. In order to model the motion of a swimming robot in an unbounded fluid, here, we use a relatively
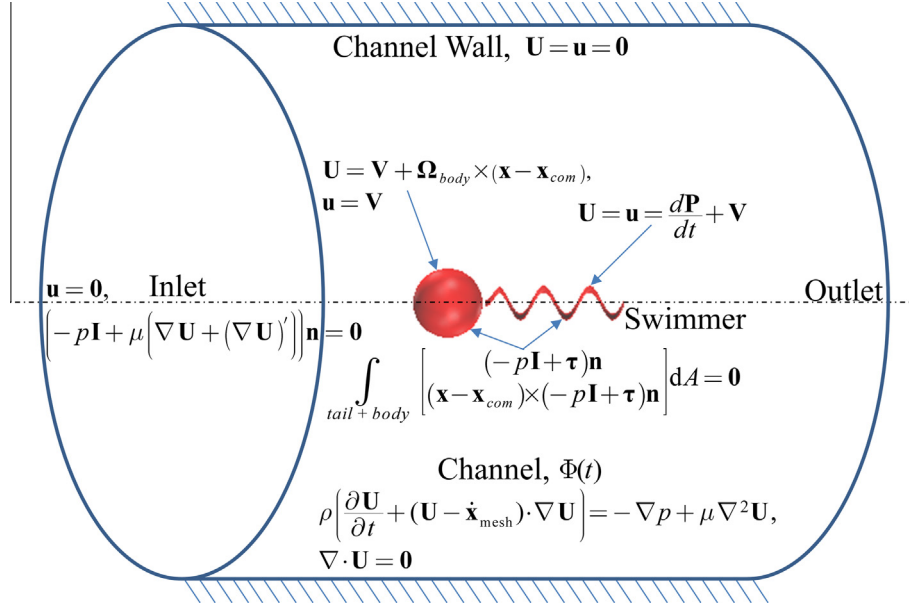
Fig. 2. Swimmer in the channel: governing equations, i.e., Navier–Stokes, subject to continuity and ALE deformation with respective boundary conditions exerted on each moving or stationary surface of the viscous medium, $\Phi(t)$.

large channel around the swimmer with the diameter as large as ten times the diameter of the body, and length five times the total length of the swimmer with negligible distortion to the flow field nearby the swimmer (see Fig. 2).

Fluid forces are calculated from the finite-element method solution of incompressible Navier–Stokes equations subject to continuity in the moving domain due to the motion of the tail and the overall swimmer, and arbitrary Lagrangian Eulerian (ALE) scheme [27] is used in order to handle the deforming mesh as given in Eq. (12). Equations are written in dimensionless form with the diameter of the body, D_{body}, as the length-scale and $2\pi/\omega$ as the time-scale; hence, the velocity-scale is $\omega D_{body}/2\pi$, which varies linearly with the frequency, and the final scaling Reynolds number is found to be Re = $\rho\omega (D_{body})^2/2\pi\mu$. Complete list of variables used in the representative base-case design is shown in Table 1.

$$\rho\left(\frac{\partial \mathbf{U}}{\partial t} + (\mathbf{U} - \dot{\mathbf{x}}_{mesh}) \cdot \nabla \mathbf{U}\right) = -\nabla p + \mu\nabla^2\mathbf{U},$$
$$\nabla \cdot \mathbf{U} = 0. \tag{12}$$

The boundary conditions imposed on stationary and moving boundaries are depicted in Fig. 2. Fluid and mesh deformation velocities, i.e., $\mathbf{U}$ and $\mathbf{u}$, are set to zero on channels walls to ensure no-slip boundary conditions and constant channel geometry during time-dependent solution of the governing equations. Akin to

Table 1
Parameters and their dimensionless values for the base-case swimmer studied with the CFD model.

Parameter name	Dimensionless value
Radius of the spherical body, r_{body}	0.5
Chord radius of the tail, r_{tail}	0.05
Apparent tail length, L	2
Apparent wavelength, λ	2/3
Wave amplitude, b	0.1
Actuation frequency of the tail, $\omega/2\pi$	1
Fluid density, ρ	1
Scaling Reynolds number, Re = $\rho\omega(D_{body})^2/2\pi\mu$	10^{-2}
Channel length, L_{ch}	10
Channel diameter, $2r_{ch}$	10
Spherical body resistance coefficients, $\{6\pi\mu r_{body}, 8\pi\mu(r_{body})^3\}$	$\{942.5, 314.2\}$

the walls, mesh deformation is completely restricted at the inlet and outlet of the channel; however, the hydrodynamic stress vector is set to zero to ensure open-boundary condition on both sides with the following set of equations:

$$(-p\mathbf{I} + \mu(\nabla\mathbf{U} + (\nabla\mathbf{U})'))\mathbf{n} = 0,$$
$$\mathbf{U} = 0. \tag{13}$$

The velocity boundary conditions on the surface of the body are given in Eq. (14), and the velocity boundary conditions on the surface of the tail are specified in Eq. (15). It is noted that the mesh velocity $\mathbf{u}$ on the body surfaces does not incorporate its $\mathbf{s}$-rotation due to symmetry of the spherical geometry.

$$\mathbf{U}_{body} = \mathbf{V} + \mathbf{\Omega}_{body} \times (\mathbf{x} - \mathbf{x}_{com}),$$
$$\mathbf{U}_{body} = \mathbf{V}. \tag{14}$$

$$\mathbf{U}_{tail} = \mathbf{U}_{tail} = \frac{d\mathbf{P}}{dt} + \mathbf{V}. \tag{15}$$

Here, $\mathbf{x}$ is local the position vector, and $\mathbf{x}_{com}$ is the position of the center of mass, which is assumed to be the geometric center of the spherical body. Hydrodynamic forces on the swimmer are computed from the integration of the stress distribution over the surface of the swimmer, and set to zero in order to satisfy force-free swimming constraints [23] and obtain swimming velocities with proper no-slip moving boundary conditions, i.e., Eq. (11) imposed on body surfaces and Eq. (7) imposed on tail surfaces, as follows:

$$\begin{bmatrix}\mathbf{F}\\\mathbf{T}\end{bmatrix}_{tail} + \begin{bmatrix}\mathbf{F}\\\mathbf{T}\end{bmatrix}_{body} = \begin{bmatrix}\int_{tail+body}\boldsymbol{\sigma}\mathbf{n}\ dA\\\int_{tail+body}(\mathbf{x} - \mathbf{x}_{com}) \times \boldsymbol{\sigma}\mathbf{n}\ dA\end{bmatrix} = 0. \tag{16}$$

Here, $\boldsymbol{\sigma}$ is the total fluid stress tensor with pressure, p, and shear, τ, terms such that $\boldsymbol{\sigma} = -p\mathbf{I} + \tau$. Time-dependent three-dimensional local surface normal is denoted by the vector $\mathbf{n}$. Rigid-body translations of the swimmer and the rotation of the body along the $\mathbf{s}$-axis are obtained by means of Eq. (16), which is analogous to Eq. (1). The numeric procedure, i.e., the two way coupling between hydrodynamic forces and rigid body kinematics, used in the commercial software COMSOL Multiphysics [28] to calculate the swimmer velocity vector is presented in Algorithm 1.

Here we did not take the lateral rotations of the swimmer into account by simply excluding corresponding constraints from the solution given the fact that helical tail and body are collinear [29].

Algorithm 1. Calculating time-dependent swimming velocity vector in COMSOL Multiphysics.

1	**do**
2	**if** $t = 0$ **then**
3	Initialize: $\mathbf{V}(t = 0) = \mathbf{0}$ & $\mathbf{u}(t = 0) = \mathbf{0}$ & $\boldsymbol{\sigma}(t = 0) = \mathbf{0}$ & $\omega(t = 0) = 2\pi f$.
4	**else**
5	$\omega = 2\pi f$
6	Compute the total hydrodynamic force induced with the helical tail by its rotation with the angular velocity, ω, and by the swimmers' rigid body velocity vector, $\mathbf{V}$.
7	Compute the rigid body velocity vector $\mathbf{V}$ that would satisfy the constraint equations $\mathbf{F}_{body} + \mathbf{F}_{tail} = \mathbf{0}$ and $\mathbf{T}_{body} + \mathbf{T}_{tail} = \mathbf{0}$.
8	**end**
9	Update surface velocity boundary conditions on the helical tail with computed swimming velocities, i.e., $\mathbf{U} = \mathbf{V} + d\mathbf{P}/dt$, and update the surrounding mesh with ALE, for the consecutive time increment, $t = t + \delta t$.
10	Update the velocity on the moving/deforming surfaces of the swimmer
11	**while** $t \leqslant t_{final}$

CFD simulations are carried out for the left-handed helical tail rotating in the positive direction with respect to the **s**-coordinate as shown in Fig. 1. Commercial software COMSOL Multiphysics [28], which is based on the finite-element method, is used to perform the simulations with the second order Lagrangian tetrahedral elements with 300,000 dof. Linear system of equations is solved with the PARDISO linear solver [30] and a second order backward difference formula with variable time-stepping for the numerical integration in time (maximum time step is set to 0.0025). Simulations require up to twenty hours on a high-end workstation in order to complete two full periods of the wave propagation on the tail depending on its geometric parameters. In effect, the CFD model is employed to verify our novel approach to use a single set of constant force coefficients for a range of design parameters.

We used a similar CFD model in [17] to obtain an improved resistance matrix for the body which predicts the time-dependent hydrodynamic forces accurately as opposed to conventional RFT method. The improved resistance matrix approach incorporates complex-impedance analysis leading to amplitude and phase-angle corrections which are essential to obtain the time-dependent velocity vector and the trajectory of the swimmer. However, in [17], corrections are obtained for each individual swimmer in a limited design space; a task proved to be laborious due to numerical stiffness, mesh generation issues, and convergence problems. Although amplitude correction is employed extensively to achieve accurate prediction of the time-averaged hydrodynamic forces in this study, the procedure is carried out only once for a single geometric design of choice along with calculation of the local resistance coefficients of the tail constituting a unique set of coefficients together which then validated in respect of accuracy against a set of CFD simulations by means of time-averaged quantities. Further discussion on the CFD model with validation by means of in-channel swimming experiments is provided by Tabak and Yesilyurt [17].

3. Results

3.1. Validation of the hydrodynamic model with measurements

Hydrodynamic surrogate model is compared against measurements reported in literature. Resistance coefficients from Lighthill's SBT analysis [12] are used for the helical tail in this part.

Goto et al. [15] measured forward velocity and body rotation rates for a number of specimens of *V. Alginolyticus*, whose dimensions and tail rotation rates vary. Authors could not measure the frequency of rotations of the helical tail, due to relatively high frequency of tail rotations compared to body rotations, and used a BEM model to calculate the tail-rotation frequency from the measured frequency of body rotations. Table 2 shows reported [15] geometric parameters of individual organisms: for all cases, radius of the tail is 16 nm, wavelength of the helical waves is 1.37 μm and the amplitude, i.e., the helical radius, is 0.1487 μm.

Translational and rotational resistance coefficients of the body in the swimming direction (see **s**-direction in Fig. 1) are calculated with the use of drag coefficients for oblique spheroids [22] from:

$$\mathbf{D}_{N,s} = \Gamma_{N,s} 4 \Pi \mu r_s / (\log(2r_s/r_q) - 0.5), \tag{17}$$

$$\mathbf{D}_{R,s} = \Gamma_{R,s} (16/3) \Pi \mu r_s r_q^2. \tag{18}$$

In Eqs. (17) and (18), $r_{\{s,q\}}$ denote the radii of the body in the **s**- and **q**-directions respectively, and $\Gamma_{\{N,R\},s}$ are the hydrodynamic interaction coefficients, that correspond to the deviations in the fluid resistance acting on the isolated body ideally submerged in an unbounded fluid. In essence, interaction coefficients quantify variations in translational and rotational body drag coefficients due to the flow field realized by the rotating tail attached to the body: if interaction coefficients in Eqs. (17) and (18) are set to unity, translational and rotational drag factors, $\mathbf{D}_{N,s}$ and $\mathbf{D}_{R,s}$, would be those of isolated spheroids in infinite media.

Time-averaged forward velocity and the body-rotation rate of natural swimmers are calculated from Eq. (11) and compared with the measurements of Goto et al. [15] in Fig. 3. There is a significant discrepancy between the measurements and model results when interaction coefficients are set to unity, i.e., for $\Gamma_{\{N,R\},s} = 1$: maximum error is 87% in the average forward velocity for specimen-G, and 47.2% in the body-rotation rate for specimen-B.

Values of two interaction coefficients, $\Gamma_{N,s}$ and $\Gamma_{R,s}$, can be determined from the solution of the inverse problem for observed values of the forward velocity and the body rotation rate of a selected swimmer as the representative design. Here, specimen-C is used as the representative design of choice due to lowest margin of error in the measurements, and the interaction coefficients in translational and rotational drag relationships given by Eqs. (17) and (18) are calculated as $\Gamma_{N,s} = 2.37$ and $\Gamma_{R,s} = 1.49$, respectively, from the solution of the inverse problem. As shown in Fig. 3, the agreement between the hydrodynamic model and measurements

Table 2
Geometric parameters of selected *V. alginolyticus* specimens [15].

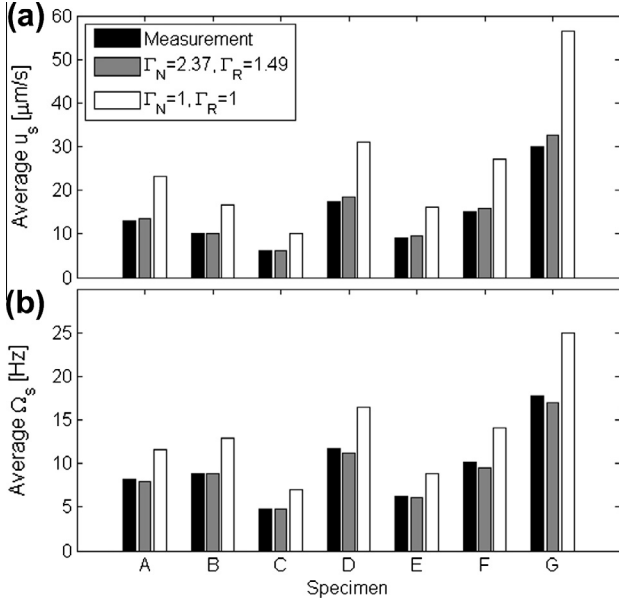| Specimen	Frequency (Hz)	Tail length (μm)	Body **s**-semi-axis, r_s (μm)	Body **q** and **r**-semi-axes r_q (μm)
A	187.70	4.89	1.885	0.415
B	123.20	4.90	1.320	0.380
C	73.95	5.24	1.380	0.405
D	244.70	5.19	1.975	0.400
E	126.20	5.03	1.785	0.405
F	220.10	5.07	2.260	0.380
G	477.10	4.87	2.280	0.410

Fig. 3. Comparisons on: the time-averaged forward velocity (a); and angular velocity of the body (b); between the measurements reported by Goto et al. [15] and the surrogate model results with unmodified and corrected body drags.

is very good with updated resistance coefficients of the body: maximum error is 8.2% in the average forward velocity for specimen-G, and 6.5% in the body rotation rate for specimen-F.

Despite that the selected specimens have different body, tail and wave configurations (see Table 2), interaction coefficients obtained from the solution of the inverse problem for an arbitrary selected specimen work very well with other specimens as well. Furthermore, agreements of results with specimens-A, B and E are remarkable; therefore, specimens-A, B, C and E have similar hydrodynamic interactions, and using anyone of them as the representative case would not make any difference. Thus, once the resistance coefficients of the body are obtained accurately, the surrogate model would perform sufficiently well in subsequent analyses.

3.2. CFD simulations

3.2.1. Estimation of resistive force coefficients and hydrodynamic interaction corrections

Two sets of resistance coefficients are used in the hydrodynamic model: the first set is by Lighthill [12] and obtained from Eqs. (5) and (6), and the second set is obtained from the CFD simulation for a stationary swimmer. The helical radius, i.e., wave amplitude, of the tail is set to 0.1 and the wavelength to 2/3 as the base case design. Complete list of base-case design parameters and their values are listed in Table 1.

Stationary swimmer in the CFD simulation is not subject to force-free swimming constraints given by Eq. (16), thus the rotating left-handed helical tail generates a net propulsion force in the opposite direction of the helical-wave propagation. The propulsion force and the propulsion torque on the swimmer's body can be calculated from the integration of the stress field over the tail in the CFD model. Then, integrations on the right-hand-side of Eq. (10) are carried out explicitly only in the swimming direction (see **s**-direction in Fig. 1) to obtain a closed-form expression for the force and the torque generated by the tail and the rotation and the translation velocities as follows:

$$\begin{bmatrix} \overline{F}_{tail,s} \\ \overline{T}_{tail,s} \end{bmatrix} = -\alpha L \left\{ \begin{bmatrix} b^2 k^2 & 1 \\ b^2 k & -b^2 k \end{bmatrix} \bar{u}_s + \begin{bmatrix} k & -k \\ 1 & b^2 k^2 \end{bmatrix} b^2 \omega \right\} \begin{bmatrix} c_n \\ c_t \end{bmatrix}. \quad (19)$$

where $\alpha = (1 + b^2 k^2)^{-1/2}$ is the ratio of the apparent length of the helix to the actual rod length of the tail. Here, b is the helical radius, which is 0.1 for the base case, k is the wave number, which is 3 for the base case, $\bar{u}_s$ is the average swimming speed, which is zero for the stationary swimmer, and ω is the frequency of rotations of the tail. Once the left-hand-side of Eq. (19) is computed from the CFD model for the stationary swimmer, resistance coefficients, $c_{\{n,b\}}$ and c_t are, then, easily calculated as 995.5 and 775.2, respectively. Arguably, the constant pair of force coefficients, which are obtained from the CFD simulation, incorporates realistic flow conditions such as the trailing-edge force due to the motion of the tip of the tail, which is not taken into account in the derivation of the resistance coefficients from the SBT [12].

Resistance coefficients of the body are obtained from the well-known drag coefficients of spherical objects, which are multiplied by translational and rotational hydrodynamic interaction coefficients, $\gamma_{N,\{s,q,r\}}$ and $\gamma_{R,\{s,q,r\}}$, respectively, as:

$$\mathbf{D}_N = 6\Pi \mu r_{body} \begin{bmatrix} \gamma_{N,s} & 0 & 0 \\ 0 & \gamma_{N,q} & 0 \\ 0 & 0 & \gamma_{N,r} \end{bmatrix}, \quad (20)$$

$$\mathbf{D}_R = 8\Pi \mu r_{body}^3 \begin{bmatrix} \gamma_{R,s} & 0 & 0 \\ 0 & \gamma_{R,q} & 0 \\ 0 & 0 & \gamma_{R,r} \end{bmatrix}. \quad (21)$$

Furthermore, strictly-diagonal form of the body resistance matrix, which is considered here, can be viewed as an alternative to a general full-matrix of fluid resistance that includes all hydrodynamic interactions and is investigated for real-time trajectory prediction and planning purposes elsewhere [17].

For helical propulsion, only one translational correction in lateral directions, i.e., $\gamma_{N,q} = \gamma_{N,r}$, is necessary due to flow symmetry, along with the correction for forward translation, $\gamma_{N,s}$, and the correction for the body rotation, $\gamma_{R,s}$, given the fact that lateral rigid-body rotations are eliminated for simplicity in the numerical procedure.

Interaction coefficients for the spherical body of the free swimmer that corresponds to the base-case representative design are calculated directly from the ratio of forces and velocities obtained from the CFD simulation. Time-dependent forward velocity of the swimmer is nearly constant, i.e., −0.038, varying within 0.6% of its average value. The net hydrodynamic drag force in the swimming direction on the spherical body of swimmer is obtained as 81.7, which corresponds to 2.28 times the well-known drag force on spherical objects. Therefore, the interaction coefficient in the swimming direction is obtained as, $\gamma_{N,s}^{CFD}$ = 2.28. Similarly, the angular velocity of the swimmer is almost constant, i.e., −0.4, varying within 0.2% of its time-averaged value, and the torque exerted on the spherical body is 1.09 times its well-known value for spherical objects and sets the value interaction coefficient for rotations in the swimming direction as $\gamma_{R,s}^{CFD}$ = 1.09.

Lateral (see **q**- and **r**-directions in Fig. 1) velocities and forces are sinusoidal in time with zero mean and amplitude of 0.015 and 7.235, respectively. Here, we use the interaction coefficient from the solution of the inverse problem and obtained as $\gamma_{N,q}^{CFD} = \gamma_{N,r}^{CFD}$ = 1.24 based on the amplitudes of the lateral forces and the lateral velocities.

Calculated values of interaction coefficients vary with the choice of resistance coefficients used for the tail, since the effect of hydrodynamic interactions between the body and the tail is evaluated by the interaction coefficients applied only to body resistances. Therefore, a new set of interaction coefficients is necessary for the resistance coefficients obtained from Lighthill's SBT [12]. In this case, we solve the inverse problem, i.e., Eq. (11), for already calculated velocities and obtain interaction coefficients for the
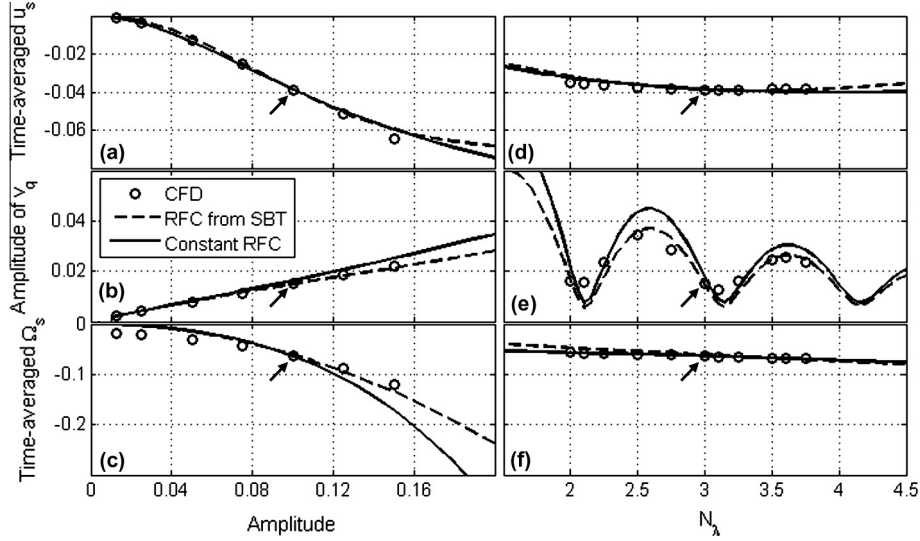
Fig. 4. Time-averaged forward velocity (a) and (d); amplitude of the lateral velocity (b) and (e); and rotation of the body (c) and (f): against, the wave amplitude (a)–(c); and number of waves (d)–(f). The circles (○) signify CFD results, the solid lines (–) are for hydrodynamics model with resistance coefficients obtained from the CFD simulation for a stationary swimmer, and dashed lines (– –) are for hydrodynamic model results with resistance coefficients obtained from Lighthill's SBT analysis [12]. Black arrows point data points corresponding to the base-case design.

body resistance matrices, which are calculated as $\gamma_{N,s}^{SBT} = 3.35$, $\gamma_{N,q}^{SBT} = \gamma_{N,r}^{SBT} = 1.1$, and $\gamma_{R,s}^{SBT} = 0.85$.

3.2.2. Validation of the hydrodynamic model with CFD simulations

The hydrodynamic model is validated with additional CFD simulations for swimmer tails with different amplitudes and wavelengths than the ones used in the representative design, which is used for the estimation of interaction coefficients for the body and resistance coefficients for the tail. Here, we considered only the wavelength and amplitude for clarity and conciseness as design variables of propulsion invoked by the flagellum; however, study can be extended to other parameters such as the body radius, and tail length. Moreover, frequency, diameter of the body and fluid properties are already lumped into the scaling Reynolds number used in simulations: for small Reynolds numbers, the velocity of the robot scales linearly with the frequency of tail rotations and its body size.

For swimmers with helical tails, hydrodynamic model results are compared with CFD simulation results in Fig. 4(a)–(f). Average forward velocity (see Fig. 4(a)), amplitude of the lateral velocity (see Fig. 4(b)) and the body rotation rate (see Fig. 4(c)) are plotted against the wave amplitude. According to the results obtained by the surrogate model with resistance coefficients from Lighthill's SBT [12], magnitude of the time-averaged forward velocity increases with the amplitude with a rate that slows down at higher values. The model results with CFD-based force coefficients also show that the average velocity increases with the amplitude. In this case, a slightly better agreement with actual simulation results is observed than the case with SBT-based force coefficients. The agreement between the hydrodynamic surrogate model and simulation results is better at small values of the amplitude than large ones (see Fig. 4(a)), thus, indicating that as the helical radius increases and the flow induced by the tail gets stronger than the case used for the estimation of interaction coefficients the accuracy of the surrogate model deteriorates.

Time-dependent lateral motion of the swimmer is periodic with zero mean-value. However, the amplitude of the lateral velocity increases almost linearly with the amplitude of the helical waves. The agreement is slightly better for the force coefficients from the SBT than the force coefficients obtained from the CFD simulation for the stationary swimmer (see Fig. 4(b)). Similarly, in Fig. 4(c),

model results with analytically obtained force coefficients from SBT agree with simulation results for large wave amplitudes better than the results with constant force coefficients, i.e., 11.8% error vs. 42.7% error; agreement is poorer for both sets of coefficients at small amplitudes.

Average forward velocity, amplitude of the lateral velocity and the average body rotation rate are plotted against the number of waves in Fig. 4(d)–(f), respectively. The forward velocity predicted by the hydrodynamic model indicates that the wavelength does not have a significant effect, and agrees well with CFD simulation results for both sets of parameters as depicted in Fig. 4(d) (with 6.9% error for constant $c_{\{n,b\}}$ and c_t, and with 9.3% error for $c_{\{n,b\}}$ and c_t from the SBT). The amplitude of the lateral velocity peaks at half integer values of the number of waves, i.e., for $N_\lambda = 0.5$, 1.5, 2.5, 3.5, etc., and falls at full integer values, which is already confirmed in [22]. When the helical waves are in full-periods, forces in the lateral directions are minimal due to hydrodynamic symmetry.

Overall, the hydrodynamic model predicts the lateral motion well especially with analytical resistance coefficients compared to resistance coefficients computed from the CFD simulation for the stationary swimmer (see Fig. 4(e)). Lastly, the rotation rate of the body does not vary with the number of waves on the tail significantly, and is predicted reasonably well with the hydrodynamic model as shown in Fig. 4(f).

Summary of the performance of the hydrodynamic surrogate model is presented in Table 3. Overall, the surrogate model agrees very well with CFD model results for both sets of resistance coefficients used in the model.

4. Surrogate model for efficient geometric designs

Here, a representative demonstration of the use of surrogate model for design purposes is presented: geometric design of a robotic micro-swimmer system, e.g. bio-mimetic robots [5–7], genetically modified cells for specific tasks [31], or cybernetic combinations of computers and bacteria [8,9,32], can be carried out with the validated surrogate model that can replace the computationally exhaustive three-dimensional CFD model. For instance, energy consumption of the robot, for which the base case parameters are given in Table 1, can be minimized with the maximization of its efficiency. Efficiency is given by:

Table 3
Errors in predictions of the hydrodynamic model, (absolute error, error range).

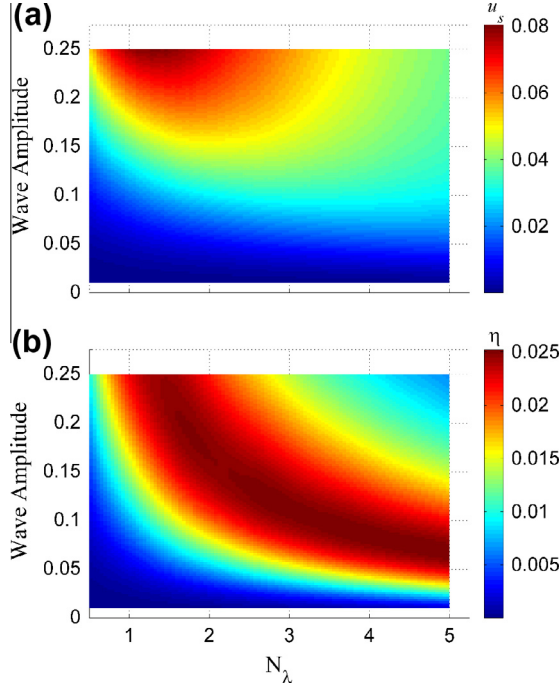|	Number of waves		Amplitude	
	CFD-based constant $c_{\{n,b\}}$, c_t	Analytical $c_{\{n,b\}}$, c_t	CFD-based constant $c_{\{n,b\}}$, c_t	Analytical $c_{\{n,b\}}$, c_t
$\bar{u}_s$	.0025, $[-.0327, -.0393]$	.0033, $[-.0319, -.03939]$	.0047, $[-.0011, -.0596]$	.0046, $[-.0008, -.0597]$
$v_{q,max}$	.0085, $[.0073, .0435]$	.0102, $[.0052, .0356]$	.003, $[.002, .0251]$	.00074, $[.002, .0212]$
$\bar{\Omega}_s$	.0011, $[-.0574, -.0694]$	.00843, $[-.0708, -.4783]$	.0516, $[-.0009, -.1722]$	.00143, $[-.0009, -.1349]$

Fig. 5. Time-averaged forward velocity, u_s, (a); and hydrodynamic efficiency, η, (b); obtained by the surrogate model. Highest possible hydrodynamic efficiency for the proposed geometric design space is 2.5% (dark red region in (b)). (For interpretation of the references to colour in this figure legend, the reader is referred to the web version of this article.)

$$\eta = \frac{\Pi_{body}}{\Pi_{tail}}. \tag{22}$$

where $\Pi_{body} = F_s u_s$ is the average rate of work done to move the body of the robot with the velocity of u_s against the drag force on the body, F_s, and Π_{tail} is the rate of work done to actuate the tail of the robot and calculated from $\Pi_{tail} = T_s \omega$ for helical tails, where T_s denotes the torque needed to rotate the tail with angular velocity, ω.

Time-averaged forward velocity (see Fig. 5(a)) and the hydrodynamic efficiency of swimmers (see Fig. 5(b)) are calculated with the surrogate model for amplitudes varying between 0.01 and 0.25 and for number of waves varying between 0.5 and 5. According to Fig. 5(a), the maximum velocity of 0.08 is computed for $b = 0.25$ and $N_\lambda = 1.25$. Therefore, in order to manufacture a swimmer with the fastest forward velocity within the predefined design space depicted by Fig. 5, one has to build a tail with one and a quarter helical turn and the largest possible amplitude. Furthermore, from Fig. 5(b), the maximum efficiency is obtained as 2.5% for the robots with parameters as presented in Table 1. It is noted that Fig. 5 is composed of data points more than a thousand which would require an overwhelming time to carry out the CFD simulations provided that numerical convergence and meshing issues are completely resolved; however, with the validated RFT model it takes only a couple of hours to obtain a surface such as depicted

in Fig. 5 for design and optimization purposes. Moreover, the RFT model can be directly invoked by formal search algorithms, such as steepest descent, if necessary.

Furthermore, it is known that the presence of channel walls alters the induced flow field around the swimmer [33] and the hydrodynamic force acting on the swimmer [34,35]. Here, the RFT-based model is employed to investigate hydrodynamic efficiency and speed of free swimmers. Therefore, swimming near boundaries requires a separate study to obtain a constant set of force coefficients that would serve as a surrogate for a limited design space.

5. Conclusions

Time-averaged forward translation and rotation with maximum instantaneous lateral translation of bio-inspired micro-swimmers that consist of a body and an actuated helical tail are predicted with the surrogate model, which is based on a number of parameters used in the linear relationship between the force and velocity vectors. The hydrodynamic model runs essentially in real-time unlike the three-dimensional CFD model that completes the solution of the governing equations in hours.

Two sets of resistance coefficients are used for the actuated tail of the swimmer: one set is from the SBT analysis of Lighthill [12], and the second set is directly calculated from a representative CFD simulation for a stationary swimmer with a helical tail for which the amplitude and wavelength are set to 0.1 and 2/3, respectively in non-dimensional units. For each set of force coefficients, hydrodynamic interaction coefficients are estimated for the body of the swimmer from the solution of the inverse problem for the base-case values of the amplitude and the wavelength. Then the hydrodynamic model is validated directly with parameterized CFD model results for swimmers, for which the wavelength is varied between 0.5 and 1 and the amplitude is varied between 0.01 and 0.15. For all cases, the surrogate hydrodynamic model results agree reasonably well with CFD model results. Moreover, variations on wave amplitude, b, also imply variations on the amplitude to body diameter ratio, i.e., b/D_{body}. Therefore, one may conclude from Fig. 4(a)–(c) that swimming velocities converge to zero as the body diameter becomes relatively larger and *vice versa*; a natural result of hydrodynamic forces acting on the body combined with equation of motion.

Furthermore, experimentally measured time-averaged forward velocity and body rotation rates for certain micro-organisms that are presented in literature are compared with the results of the hydrodynamic model with resistance coefficients obtained from SBT. Once the hydrodynamic interaction coefficients of the body are determined from the inverse problem for a fixed specimen, predicted forward velocities and body rotation rates agree very well with the measurements for other species with different body and tail dimensions.

Lastly, we demonstrated the application of validated surrogate models in geometric design of bio-mimetic robots to obtain optimal propulsion type. Therefore, optimal geometric configurations can be easily determined for various application purposes with the help of the surrogate-based approach. Based on the resistance

coefficients and hydrodynamic interaction corrections obtained from a single representative CFD simulation, it is possible to operate within a predefined design space in the neighborhood of that representative design. It is also noted that the surrogate model is a suitable tool to be incorporated in more sophisticated search algorithms as auxiliary tools for optimal design.

Moreover, in order to ensure the accuracy of the surrogate model calculations in a much larger design space, one may coarsely discretize the region of interest such that CFD simulations can be utilized to obtain correction coefficients at selected few local base-case design points. Then the surrogate model can be utilized perform computations in the neighborhood of the nodes with a much finer resolution as the study may demand.

References

[1] Martel S, Felfoul O, Mathieu JB, Chanu A, Tamaz S, Mohammadi M, et al. MRI-based medical nanorobotic platform for the control of magnetic nanoparticles and flagellated bacteria for target interventions in human capillaries. Int J Robot Res 2009;28(9):1169–82.

[2] Nelson BJ, Kaliakatsos IK, Abbott JJ. Microrobots for minimally invasive medicine. Ann Rev Biomed Eng 2010;12:55–85.

[3] Purcell EM. Life at low Reynolds number. Am J Phys 1977;45(1):3–11.

[4] Honda T, Arat KI, Ishiyama K. Micro swimming mechanisms propelled by external magnetic fields. IEEE T Magn 1996;32(5):5085–7.

[5] Zhang L, Abbott JJ, Dong L, Kratochvil BE, Bell D, Nelson BJ. Artificial bacterial flagella: fabrication and magnetic control. Appl Phys Lett 2009;94(6):064107.

[6] Zhang L, Peyer KE, Nelson BJ. Artificial bacterial flagella for micromanipulation. Lab Chip 2010;10(17):2203–15.

[7] Ghosh A, Fischer P. Controlled propulsion of artificial magnetic nanostructured propellers. Nano Lett 2009;9(6):2243–5.

[8] Martel S, Tremblay CC, Ngakeng S, Langlois G. Controlled manipulation and actuation of micro-objects with magnetotactic bacteria. Appl Phys Lett 2006;89(23). 233904-3.

[9] Martel S, Mohammadi M. A robotic micro-assembly process inspired by the construction of the ancient pyramids and relying on several thousand flagellated bacteria acting as micro-workers. In: Proceedings of the IEEE/RSJ Int Conf Intel Robots Syst, St. Louis, MO, USA; 2009.

[10] Gray J, Hancock GJ. The propulsion of sea-urchin spermatozoa. J Exp Biol 1955;32(4):802–14.

[11] Hancock GJ. The self-propulsion of microscopic organisms through liquids. Proc R Soc Lond A 1953;217(1128):96–121.

[12] Lighthill J. Flagellar hydrodynamics: the John von Neumann Lecture, 1975. SIAM Rev 1976;18(2):161–230.

[13] Higdon JJL. A hydrodynamic analysis of flagellar propulsion. J Fluid Mech 1979;90(4):685–711.

[14] Ramia M, Tullock DL, Phan-Thien N. The role of hydrodynamic interaction in the locomotion of microorganisms. Biophys J 1993;65(2):755–78.

[15] Goto T, Masuda S, Terada K, Takano Y. Comparison between observation and boundary element analysis of bacterium swimming motion. JSME Int J C 2001;44(4):958–63.

[16] Lauga E, DiLuzio WR, Whitesides GM, Stone HA. Swimming in circles: motion of bacteria near solid boundaries. Biophys J 2006;90(2):400–12.

[17] Tabak AF, Yesilyurt S. Improved kinematic models for two-link helical micro/nanoswimmers. IEEE T Robot [SI Nanorobot] 2014;30(1):14–25.

[18] Keller J, Rubinow SI. Swimming of flagellated microorganisms. Biophys J 1976;16(2):151–70.

[19] Johnson RE, Brokaw CJ. Flagellar hydrodynamics. A comparison between resistive-force theory and slender-body theory. Biophys J 1979;25(1):113–27.

[20] Chattopadhyay S, Wu X-L. The effect of long-range hydrodynamic interaction on the swimming of a single bacterium. Biophys J 2009;96(5):2023–8.

[21] White MF. Viscous fluid flow. 3rd ed. NY: McGraw-Hill; 2006.

[22] Berg HC. Random walks in biology. Expanded ed. NJ: Princeton University Press; 1993.

[23] Taylor GI. Analysis of the swimming of microscopic organisms. Proc R Soc Lond A 1951;209(1099):447–61.

[24] Happel J, Brenner H. Low Reynolds number hydrodynamics. NJ: Prentice-Hall; 1965.

[25] Higdon JJL, Muldowney GP. Resistance functions for spherical particles, droplets and bubbles in cylindrical channels. J Fluid Mech 1995;298:193–219.

[26] Hanson AJ, Ma H. Quaternion frame approach to streamline visualization. IEEE T Vis Comput Gr 1995;1(2):164–74.

[27] Duarte F, Gormaz R, Natesan S. Arbitrary Lagrangian–Eulerian method for Navier–Stokes equations with moving boundaries. Comput Methods Appl Mech Eng 2004;193:4819–36.

[28] COMSOL AB. Comsol multiphysics modeling guide, Stockholm; 2012.

[29] Hyon Y, Marcos, Powers TR, Stocker R, Fu HC. The wiggling trajectories of bacteria. J Fluid Mech 2012;705:58–76.

[30] Schenk O, Gärtner K. Solving unsymmetric sparse systems of linear equations with PARDISO. Future Gener Comp Syst 2004;20(3):475–87.

[31] Wu HC, Tsao CY, Quan DN, Cheng Y, Servinsky MD, Carter KK, et al. Autonomous bacterial localization and gene expression based on nearby cell receptor density. Mol Syst Biol 2013;9:636.

[32] Felfoul O, Martel S. Assessment of navigation control strategy for magnetotactic bacteria in microchannel: toward targeting solid tumors. Biomed Microdev 2013;15(6):1015–24.

[33] Temel FZ, Yesilyurt S. Simulation-based analysis of micro-robots swimming at the center and near the wall of circular mini-channels. Microfluid Nanofluid 2013;14(1–2):287–98.

[34] Shum H, Gaffney EA, Smith DJ. Modeling bacterial behavior close to a no-slip plane boundary: the influence of bacterial geometry. Proc Roy Soc Lond A 2010;466:1725–48.

[35] Tabak AF, Yesilyurt S. Experimental validation of a CFD-based resistive force coefficient set for rotating helical tails in cylindrical channels. In: Proceedings of the 7th Subrata Chakrabarti Int Conf Fluid Struct Interact, Gran Canaria, Spain; 2013.